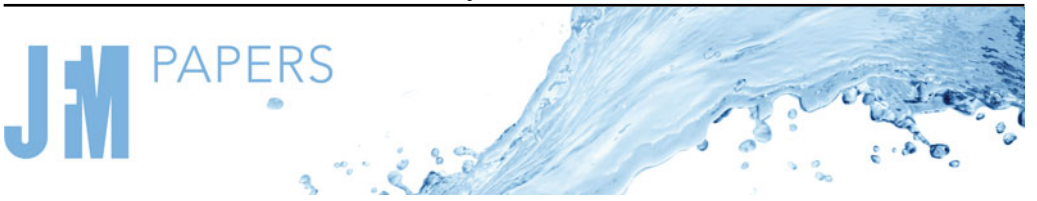
*J. Fluid Mech.* (2025), *vol.* 1025, A32, doi:10.1017/jfm.2025.10988



# Orbit dynamics of Janus drop in shear flow

**Jia-Qi Cheng**[1,†], **Chun-Yu Zhang**[1,2,†], **Jing-Wei Chen**[1], **Hao-Ran Liu**[1], **Li-Juan Qian**[2], **Peng Gao**[1] and **Hang Ding**[1]

[1]Department of Modern Mechanics, University of Science and Technology of China, Hefei 230027, PR China

[2]College of Mechanical and Electrical Engineering, China Jiliang University, Hangzhou 310018, PR China

**Corresponding authors:** Hang Ding, hding@ustc.edu.cn; Li-Juan Qian qianlj@cjlu.edu.cn

(Received 18 August 2025; revised 15 October 2025; accepted 17 November 2025)

In this paper, we numerically investigate the orbit dynamics of three-dimensional symmetric Janus drops in shear flow using an improved ternary-fluids phase field method, focusing on how drop deformation and initial orientation affect the orbit drift of two configurations of Janus drops: dumbbell-shaped and near-spherical. We find that the motion of dumbbell-shaped drops eventually evolves into tumbling, while near-spherical drops attain stable spinning. We attribute this bifurcation in orbit drift to contrasting deformation dynamics and shape-dependent hydrodynamics of the two configurations. Specifically, the drift bifurcation is closely related to the aspect ratio of Janus drops at equilibrium, giving rise to two distinct mechanisms: (1) coupling between outer interface deformation and the surrounding flow field; and (2) interplay between inner interface deformation and vortices enclosed within the drop. In addition, we observe that for the dumbbell-shaped Janus drops with different aspect ratios, their tumbling dynamics resembles ellipsoids in shear flow. Moreover, the trajectories of the dumbbell-shaped Janus drops during orbit drift collapse onto a universal curve, independent of their initial orientations, and significant deformation and inertia accelerate the orbit transition. To quantitatively evaluate the effect of drop deformation on the orbit drift of the dumbbell-shaped Janus drops, we propose an effective aspect ratio model based on the drop shapes at equilibrium and at the maximum elongation. By incorporating the effective aspect ratio into Jeffery's theory for solid particles, we accurately predict the rotation period and angular velocity of Janus drops in the tumbling regime and during the orbit drift, especially for drops with linear deformation. Moreover, the orbit parameter $C$ is found to vary exponentially with time for drops with linear deformation, while the time variation of $C$ transits from one exponential function to another for drops with nonlinear deformation.

**Key words:** drops, capillary flows

[†]The authors contributed equally to the article.

© The Author(s), 2025. Published by Cambridge University Press.



https://doi.org/10.1017/jfm.2025.10988 Published online by Cambridge University Press

## 1. Introduction

The motion of dispersed particles in shear flow can have very different trajectories. A well-known result is Jeffery orbits, which refers to the closed orbits of rotating ellipsoids in linear shear flows. When inertia of both the fluid and the particle are negligible, the Jeffery orbits can be described by the ellipsoid's aspect ratio $\lambda$, ambient shear rate $\dot{\gamma}$, polar angle $\theta$ and azimuthal angle $\phi$ (Jeffery 1922; Leal 1980; Voth & Soldati 2017)

$$\tan\theta = \frac{C\lambda}{\left(\sin^2\phi + \lambda^2\cos^2\phi\right)^{1/2}}, \quad \tan\phi = \lambda\tan\left(\frac{\dot{\gamma}t}{\lambda+\lambda^{-1}}\right), \tag{1.1}$$

where $C$ is the orbit parameter and $t$ is the time, and $\theta$ and $\phi$ are defined according to the particle orientation $\boldsymbol{d}$ in the coordinate system (figure 1*a*). In principle, the rotation of ellipsoids can consist of infinite stable orbits, enveloped between a tumbling orbit in the plane perpendicular to the vorticity ($C=\infty$) and a spinning orbit parallels to the vorticity ($C=0$). However, completely inertia-free systems are rare in nature. Jeffery (1922) hypothesised that a weak inertial effect would make the particles eventually rotate around the local vorticity from the initial position. The hypothesis was soon verified by the experiments of Taylor (1923). The particles will gradually rotate from their initial orbit to a stable orbit, a process known as orbit drift. Inertia-induced orbit drift has also been verified and investigated by theoretical analysis (Subramanian & Koch 2005, 2006; Guazzelli & Pouliquen 2018), experiments (Di Giusto *et al.* 2024) and simulations (Feng & Joseph 1995; Huang *et al.* 2012). In particular, prolate particles drift towards a tumbling orbit over a few Jeffery rotations, and the increase of the orbital parameter $C$ with time is accompanied by oscillations (Mao & Alexeev 2014).

The orbit drift of particles in shear flow is closely related to the aspect ratio of their geometry. For a spheroid, the aspect ratio $\lambda$ is normally defined as the ratio between the half-length of the symmetry axis and the radius of the spheroid equator. The effect of $\lambda$ on the orbit drift of spheroids has been investigated by theoretical analysis under the assumption of weak inertia (Mao & Alexeev 2014; Einarsson *et al.* 2015; Dabade, Marath & Subramanian 2016; Marath & Subramanian 2017). Dabade *et al.* (2016) reported that prolate spheroids ($\lambda>1$) would drift towards the tumbling orbit ($C=\infty$), while oblate spheroids display a bifurcation in orbit drift at a critical aspect ratio $\lambda^*$ ($\approx$0.14). Specifically, they found that oblate spheroids with $\lambda^*<\lambda<1$ do not have a stable tumbling orbit but a stable spinning orbit, and for those with $\lambda<\lambda^*$, the eventual orbit depends on the initial polar angle. For other axisymmetric particles, Karnis, Goldsmith & Mason (1963) found experimentally that fibres ($\lambda\gg1$) and disks ($\lambda\ll1$) suspended in circular tubes would eventually rotate in the tumbling and spinning orbits, respectively. To quantitatively describe the orbit dynamics of axisymmetric particles in general, the solution of Jeffery orbit was extended by introducing an effective aspect ratio $\lambda_e$ (Trevelyan & Mason 1951), e.g. $\lambda_e=1.24\lambda/\sqrt{\log\lambda}$ for slender cylinders (Cox 1971), $\lambda_e=1.14\lambda^{0.844}$ for rod-like particles (Harris & Pittman 1975) and $\lambda_e=1.12\lambda^{0.75}$ for cylindrical disks (Singh *et al.* 2014). Furthermore, rigid particles can have chaotic orbits when they are non-axisymmetric (Yarin, Gottlieb & Roisman 1997; Thorp & Lister 2019). However, deformable particles may also rotate in shear flow, such as flexible fibres (Slowicka, Stone & Ekiel-Jezewska 2020; Bonacci *et al.* 2023) and red blood cells (Mauer *et al.* 2018). Zhang & Graham (2020) numerically observed that deformable prolate capsules in shear flow might have multiple stable orbits, especially for the capsules with large bending stiffness.

Oriented compound drops such as Janus drops can exhibit complex dynamic behaviours in shear flow. Due to their unique structure and inherent anisotropy, Janus drops display



https://doi.org/10.1017/jfm.2025.10988 Published online by Cambridge University Press

dual behaviour: they rotate like rigid ellipsoids while simultaneously deforming like conventional drops. This combination, further complicated by their fore–aft asymmetry, leads to highly complicated dynamics. As a result, Janus drops have significant potential for diverse applications such as colour displayers (Goodling *et al.* 2019), drug delivery (Song *et al.* 2021) and biomedicine (Hao *et al.* 2022). For Janus drops with 'ideal' shape (spherical with a flat, inner interface separating the two drops of equal size), Díaz-Maldonado & Córdova-Figueroa (2015) theoretically demonstrated that the drops could behave as pure drops or as solid particles with broken fore and aft symmetry. Experiments have also been conducted to study dynamical differences between Janus drops and pure drops, including drop generation via microfluidic technology (Guo *et al.* 2017; Zhu *et al.* 2023), drop breakup in bifurcating microchannels (Wang *et al.* 2024) and drop impact on substrates (Yun, Kim & Kim 2022; Hwang & Yun 2023; Jung & Yun 2023 ). In addition, Torza & Mason (1970) experimentally observed the rotation and deformation of Janus drops in shear flow. In these experiments, Janus drops are asymmetrical due to differences in surface tension, viscosity or volume between their two component drops. By contrast, numerical investigation of Janus drops in shear mainly focused on the periodic rotation and deformation of symmetric two-dimensional (2-D) drops (Liu & Park 2022; Zhang *et al.* 2023) and engulfing behaviour of three-dimensional (3-D) drops (Liu & Park 2023). Among them, Zhang *et al.* (2023) proposed a model based on Jeffery's theory to predict the rotation periods, by introducing a corrected shear rate and an effective aspect ratio for drop deformation. However, it remains unknown whether 3-D oriented compound drops encounter orbit drift similar to 3-D rigid ellipsoids, and if so, how the drop deformation and the initial polar angle would affect their orbit dynamics.

In this study, we investigate the orbit dynamics of 3-D symmetric Janus drops in simple shear flow using an improved ternary-fluid phase field model. To simplify the flow problem, we restrict our study to the Janus drop consisting of two component drops of equal size, matched density and viscosity. We focus on two equilibrium configurations: near-spherical (similar to the 'ideal' shape and characterised by significantly lower surface tension coefficient at the inner interface compared with the outer interfaces) and dumbbell-shaped (where surface tension coefficients are comparable), to evaluate the geometric effect of Janus drops on the orbit dynamics. With the help of numerical simulations, we identify the flow regimes in the range of flow parameters considered, measure the instantaneous deformation and orientation of the Janus drops in shear flow, investigate the effect of the initial polar angle and deformation of the Janus drops on their orbit dynamics, and analyse the relevant mechanisms. In particular, we propose an effective aspect ratio model and calculate the orbit parameter for dumbbell-shaped Janus drops, to quantitatively evaluate the effect of drop deformation on the orbit drift. Finally, we make predictions of the orbit dynamics of Janus drops, following the spirit of Jeffery's theory for ellipsoidal particles.

## 2. Problem statement and methodology

### 2.1. *Problem statement*

We consider 3-D numerical simulations of a neutrally buoyant Janus drop in shear flow. A sketch of the Janus drop considered and its geometry parameters are shown in figure 1($a$, $b$), in which the Janus drop consists of two immiscible component drops 1 and 2 of equal volume $2\pi R^3/3$, where $R$ is the effective radius of the component drop. The component drops (of fluids 1 and 2) and the surrounding fluid 3 have matched density ($\rho$) and viscosity ($\mu$). The surface tension coefficient at the interface between fluids $i$ and $j$ is represented by $\sigma_{ij}$. To avoid the lateral migration of Janus drops in the shear



https://doi.org/10.1017/jfm.2025.10988 Published online by Cambridge University Press

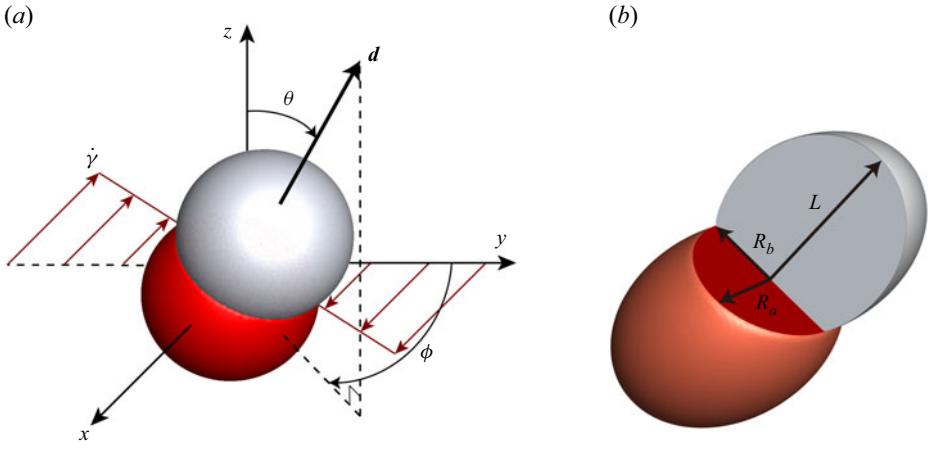



Figure 1. (*a*) A sketch of a 3-D Janus drop in simple shear flow. The vector $\boldsymbol{d}$ denotes the orientation of the Janus drop, which can be represented by the polar angle $\theta$ and azimuthal angle $\phi$ in a spherical coordinate. (*b*) Geometry measurement of drop deformation, including major semi-axis $L$, and two radii of the inner interface $R_a$ and $R_b$.

flow owing to geometric asymmetry, we consider symmetric Janus drops, particularly with $\sigma_{23} = \sigma_{13}$. Consequently, the shape of the Janus drop at equilibrium is determined by the ratio $\sigma_{12}/\sigma_{13}$, and details can be found in Appendix A. Two kinds of Janus drops at equilibrium are considered in the present study, namely dumbbell-shaped (with $\sigma_{12} \sim \sigma_{13}$; specifically, $0.347 \leqslant \sigma_{12}/\sigma_{13} \leqslant 1.532$) and near-spherical (with $\sigma_{12} \ll \sigma_{13}$).

Initially, the Janus drop is placed at the centre of a domain of $(-3R, 3R)^3$, with an undisturbed flow field $\boldsymbol{U}_0 = (\dot{\gamma} y, 0, 0)$. To maintain the shear flow, two moving plates are placed at the upper and lower boundaries at a speed of $3\dot{\gamma}R$ but in the opposite direction. Periodic boundary conditions are used in the other two directions. The dynamics of Janus drops is determined by capillary number $Ca = \mu\dot{\gamma}R/\sigma_{13}$ and Reynolds number $Re = \rho\dot{\gamma}R^2/\mu$. The orientation of the Janus drop is described by a vector $\boldsymbol{d}$, which points from the centre of mass of component drop 1 to that of component drop 2. The angle between $\boldsymbol{d}$ and the $z$-axis is defined as the polar angle $\theta$, and the azimuthal angle $\phi$ is defined as the angle between the $y$-axis and the projection of $\boldsymbol{d}$ on the $x$–$y$ plane. In the present study, we consider relatively small Janus drops, and specifically, $0.2 \leqslant Re \leqslant 1.5$ and $0.02 \leqslant Ca \leqslant 0.2$. In this range of parameters, the flow have weak inertia and Janus drops do not encounter breakup. The initial orientation of Janus drops, denoted by $\theta_0$, ranges from 0 to $\pi/2$.

### 2.2. *Numerical methods*

We employ an improved phase field model for ternary fluids to track the interface evolution (Olsson, Kreiss & Zahedi 2007; Abadi, Rahimian & Fakhari 2018; Chen *et al.* 2025). The interfaces are modelled by diffuse interfaces with finite thickness and represented by volume fractions of the fluids, $\boldsymbol{A} = (\alpha_1, \alpha_2, \alpha_3)$, where $\alpha_i$ denotes the volume fraction of the $i$th fluid, with the constraint $\alpha_1 + \alpha_2 + \alpha_3 = 1$. Time evolution of $\alpha_i$ is governed by the following equation:

$$\frac{\partial \alpha_i}{\partial t} + \nabla \cdot (\alpha_i \boldsymbol{u}) = \frac{1}{Pe} \nabla \cdot \left( \nabla \alpha_i - \frac{\alpha_i(1-\alpha_i)}{\sqrt{2}Cn} \frac{\nabla \alpha_i}{|\nabla \alpha_i|} + \frac{1}{3} \sum_{j=1}^{3} \frac{\alpha_j(1-\alpha_j)}{\sqrt{2}Cn} \frac{\nabla \alpha_j}{|\nabla \alpha_j|} \right), \tag{2.1}$$



https://doi.org/10.1017/jfm.2025.10988 Published online by Cambridge University Press

where $\boldsymbol{u}$ is the flow velocity. The Cahn number $Cn$ represents a dimensionless measure of the thickness of the interfaces (Ding, Spelt & Shu 2007). In the present study, the Cahn number is set to $Cn = 0.5h/R$, where $h$ is the mesh size. It has been shown that the Péclet number $Pe$ should obey $Pe \sim Cn^{-2}$ to ensure the sharp interface limit of the phase field model (Chen *et al.* 2025). Furthermore, to maintain the interface profile and avoid unphysical changes of interfaces, the Péclet number $Pe$ is set to $Pe = 0.007Cn^{-2}$ following the recommendation of Chen *et al.* (2025). The motion of ternary fluid flows is governed by the dimensionless continuity equation and Navier–Stokes equations,

$$\nabla \cdot \boldsymbol{u} = 0, \tag{2.2}$$

$$\rho\left(\frac{\partial \boldsymbol{u}}{\partial t} + \boldsymbol{u}\cdot\nabla\boldsymbol{u}\right) = -\nabla p + \frac{1}{Re}\nabla\cdot\left[\mu(\nabla\boldsymbol{u} + \nabla\boldsymbol{u}^T)\right] + \frac{\boldsymbol{f}_s}{ReCa}, \tag{2.3}$$

where $p$ is the pressure. The interfacial tension $\boldsymbol{f}_s$ is calculated by

$$\boldsymbol{f}_s = -\sum_{j=1}^{3}\gamma_j\nabla\cdot\left(\frac{\nabla\alpha_j}{|\nabla\alpha_j|}\right)\frac{\nabla\alpha_j}{|\nabla\alpha_j|}\delta_j, \tag{2.4}$$

where $\delta_j = 6\alpha_j(1-\alpha_j)|\nabla\alpha_j|$ is a smoothed delta function (Chen *et al.* 2025); $\gamma_j$ represents the phase-specific surface tensions and relates to the surface tension coefficients by (Zhang *et al.* 2016)

$$\begin{cases}\gamma_1 = (\sigma_{12} - \sigma_{23} + \sigma_{13})/(2\sigma_{13}),\\ \gamma_2 = (\sigma_{12} + \sigma_{23} - \sigma_{13})/(2\sigma_{13}),\\ \gamma_3 = (-\sigma_{12} + \sigma_{23} + \sigma_{13})/(2\sigma_{13}).\end{cases} \tag{2.5}$$

Details about numerical discretisation and solution procedure are available from Chen *et al.* (2025).

### 2.3. *Validation and convergence study*

We validate our simulations by comparing against experimental data from Torza & Mason (1970), where a Janus drop consisting of component droplets 1 (distilled water and 10 vol % Tween 20) and 2 (castor oil) is suspended in silicone oil (ambient fluid; $\rho_3 = 0.979\ \mathrm{kg\ m^{-3}}$, $\mu_3 = 6.4\ \mathrm{Pa\ s}$) under shear ($\dot{\gamma} = 0.106\ \mathrm{s^{-1}}$). Detailed flow conditions are listed in table 1. Due to inconsistencies between the reported volume ratio (1.125) and the experimental equilibrium drop image of Torza & Mason (1970), we set the component 1-to-2 volume ratio to 0.728 in our simulations. Surface tension coefficients were also slightly adjusted (relative error $< 3.6\,\%$) to match the experimental equilibrium shape (figure 2*a*). Although the flow in the experiment is in the Stokes regime ($Re \approx 0$), we used $Re = 0.1$ for computational efficiency, which is expected to have negligible effect on the results. In the simulation, the grid size and time step are set to $h = R/40$ and $\Delta t = 0.0002\dot{\gamma}^{-1}$, respectively. Figures 2(*b*) and 2(*c*) show the comparison between numerical results and experimental data, in terms of drop snapshots at elongation and squeeze, respectively. We can see that our numerical simulation can accurately capture the deformation and rotation of Janus drops in experiments. Furthermore, the rotation period of Janus drop is $14.47\dot{\gamma}^{-1}$ in the simulation, rather close to the experimental result of $14.20\dot{\gamma}^{-1}$.

To assess the convergence of the numerical results, we compared the drop shape at the moment of most elongation at $Re = 0.5$, $Ca = 0.2$, $\sigma_{12} = \sigma_{13}$ and $\theta_0 = \pi/2$ on progressively refined meshes, with mesh sizes of $h = R/32$, $R/40$ and $R/64$. Note that



https://doi.org/10.1017/jfm.2025.10988 Published online by Cambridge University Press

| Parameters | Unit | Experiment | Simulation |
|---|---|---|---|
| Volume of Janus drop | μL | 0.989 | 0.989 |
| Characteristic length | mm | 0.618 | 0.618 |
| $\sigma_{13}$ | mN m$^{-1}$ | 5.4 | 5.41 |
| $\sigma_{12}$ | mN m$^{-1}$ | 2.8 | 2.90 |
| $\sigma_{23}$ | mN m$^{-1}$ | 4.7 | 4.61 |
| Density ratio $\rho_1/\rho_3$ | — | Unknown | 1 |
| Density ratio $\rho_2/\rho_3$ | — | 1.006 | 1 |
| Viscosity ratio $\mu_1/\mu_3$ | — | Unknown | 0.01 |
| Viscosity ratio $\mu_2/\mu_3$ | — | 0.13 | 0.13 |
| Volume ratio $V_1/V_2$ | — | 1.125 | 0.728 |
| Capillary number | — | 0.08 | 0.08 |
| Reynolds number | — | $6.7\times10^{-6}$ | 0.1 |

Table 1. Set-up of experiments (Torza & Mason 1970) and simulation for validation.

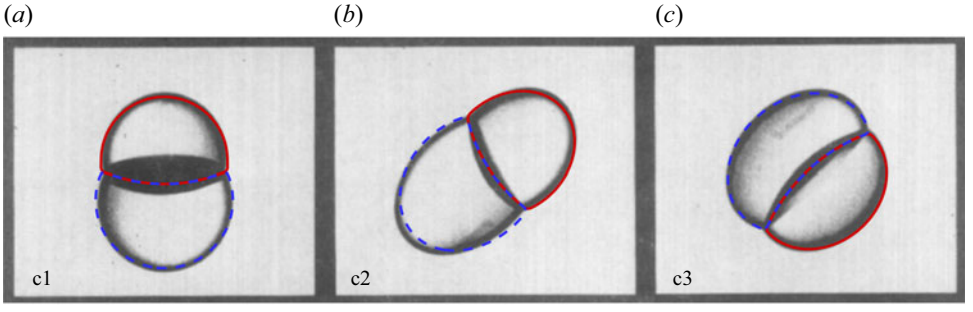



Figure 2. Snapshots of experimental observations of Janus drop in shear flow (Torza & Mason 1970) superimposed by numerical results in the $z=0$ plane (dashed lines): (*a*) drop at equilibrium; (*b*) elongation and (*c*) squeeze.

$Ca=0.2$ corresponds to the highest capillary number in this study and, thus, is expected to cause significant drop deformation. Figure 3(*a*) presents the interfaces of the Janus drop in the $x$–$y$ plane. It is clear that the profiles of the interfaces converge with the mesh refinement. In the simulations hereafter, $h=R/40$ and the time step $\Delta t=0.0002\dot{\gamma}^{-1}$ are adopted, and satisfy the computational stability when solving the equation for interface evolution, i.e. $\dot{\gamma}\Delta t<(h/R)^2$. Moreover, to assess the influence of domain boundaries, we perform two simulations at $\theta_0=\pi/2$, $Re=0.5$ and $Ca=0.2$, with the wall being positioned at $y=\pm4.5R$ and $\pm6R$, respectively. Figure 3(*b*) shows that the drop shapes for three different wall positions are virtually overlapped; this demonstrates that the wall effect can be neglected when the distance from the wall to the droplet's centre of mass exceeds $3R$.

## 3. Results and discussion

Unless stated otherwise, dumbbell-shaped Janus drop refers to the case of $\sigma_{12}=\sigma_{13}$ and near-spherical to $\sigma_{12}=0.0175\sigma_{13}$.

### 3.1. *Flow regimes: tumbling versus spinning*

Janus drops in shear flow exhibit two distinct flow regimes: tumbling and spinning. In the tumbling regime, the Janus drop continuously rotates around the direction of the



https://doi.org/10.1017/jfm.2025.10988 Published online by Cambridge University Press

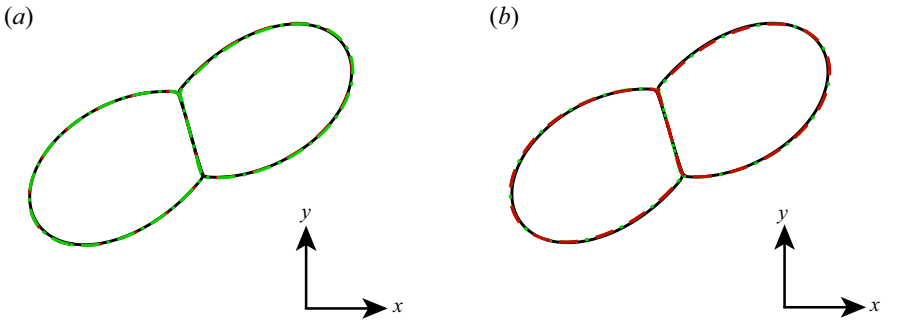



Figure 3. (*a*) Convergence study of the drop shape at the moment of most elongation at $\theta_0 = \pi/2$, $Re = 0.5$ and $Ca = 0.2$: $h/R = 1/32$ (dashed-dotted), 1/40 (dashed) and 1/64 (solid). (*b*) Comparison of drop shape at the moment of most elongation at $\theta_0 = \pi/2$, $Re = 0.5$ and $Ca = 0.2$, with the wall placed at $y = \pm 3R$ (dashed), $\pm 4.5R$ (dash-dotted) and $\pm 6R$ (solid).

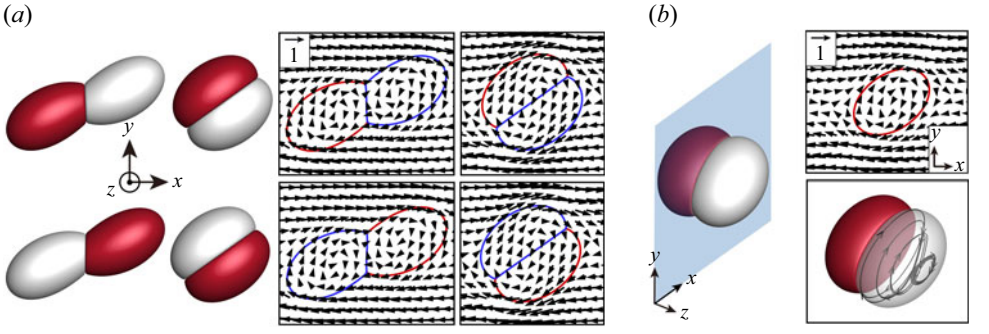



Figure 4. Dumbbell-shaped Janus drops in shear flow at $Ca = 0.2$ and $Re = 0.5$ in terms of drop snapshots and velocity vectors: (*a*) tumbling regime with $\theta_0 = \pi/2$, at times $\dot{\gamma}t = 3.2$, 10.8, 14.7, 22.3 from left to right and from top to bottom; (*b*) spinning regime with $\theta_0 = 0$ at time $\dot{\gamma}t = 15.0$, where the velocity vectors in the $x-y$ plane at $z = 0$ are shown in the top panel and streamlines in fluid 2 in the bottom panel.

vorticity of the shear flow, accompanied by periodic deformation of interfaces. By contrast, the Janus drop in the spinning regime experiences stable deformation, surrounded by steady flows and with the inner interface in the plane perpendicular to the vorticity (more precisely, the plane at $z = 0$). Figure 4 illustrates the flow regimes for the dumbbell-shaped Janus drops at $Ca = 0.2$, $Re = 0.5$ and different initial orientations $\theta_0$, with respect to interface shapes and velocity vectors. For $\theta_0 = \pi/2$, the drop falls into the tumbling regime, with a rotation period $t_R \approx 23.0\dot{\gamma}^{-1}$. Specifically, during the rotation, the outer interfaces (separating the drop from fluid 3) of the drop experience pronounced periodic deformation, while the inner interface (between the two component droplets) remains more or less flat. For $\theta_0 = 0$, the drop quickly evolves into the spinning regime (and maintains the state until the termination of computation at $\dot{\gamma}t = 200$); the flat inner interface is deformed and located in the symmetry plane, with a vortex enclosed in it.

Figure 5 depicts the flow around and the deformation of near-spherical Janus drops at $Ca = 0.02$, $Re = 0.5$ and different $\theta_0$. Similar to the dumbbell-shaped Janus drops, the near-spherical drop is tumbling at $\theta_0 = \pi/2$, while spinning at $\theta_0 = 0$. However, the deformation behaviours of the drops are very different. For example, in both regimes, the deformation of the outer interfaces resembles that of pure drops in shear flow: nearly ellipsoidal deformation under relatively weak shear ($Ca = 0.02$) and surrounded by steady

https://doi.org/10.1017/jfm.2025.10988 Published online by Cambridge University Press

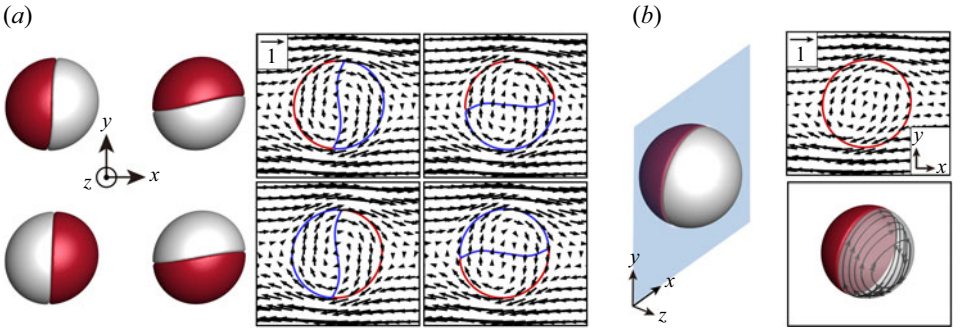



Figure 5. Dynamics of (*a*) tumbling and (*b*) spinning of near-spherical Janus drops in shear flow at $Ca = 0.02$ and $Re = 0.5$, in terms of the snapshots of interface evolution and the projected area of velocity vectors and interface shapes. In panel (*a*), $\theta_0 = \pi/2$ and the snapshots from left to right and from top to bottom correspond to $\dot{\gamma}t = 3.3, 6.4, 9.8, 12.9$, respectively. In panel (*b*), $\theta_0 = 0$ and the snapshot corresponds to the drop shape at time $\dot{\gamma}t = 15.0$, and the velocity vectors in the $x-y$ plane at $z = 0$ are shown in the top panel, while streamlines in fluid 2 in the bottom panel. In the top panel of panel (*b*), the interface represents the triple contact line where all three fluids meet.

flows. During tumbling (figure 5*a*), the inner interface rotates periodically owing to the presence of internal vortices in the Janus drop. Because for near-spherical Janus drops the surface tension coefficient of the inner interface is much lower than the outer ones, (here $\sigma_{12}/\sigma_{13} = 0.0175$), significant deformation (or even breakup) of the inner interface may occur at low $Ca$. In contrast, the spinning regime maintains a flat inner interface, which is perpendicular to the vorticity direction. Therefore, the assumption of a flat inner interface in the theoretical analysis of dynamics of spherical Janus drops (Díaz-Maldonado & Córdova-Figueroa 2015) is valid for the spinning regime, but questionable for the tumbling regime.

### 3.2. *Effect of initial orientation*

As shown in the previous section for $\theta_0 = 0$ and $\pi/2$, the initial orientation of Janus drops significantly influences the resulting flow regimes. In this section, we examine how the initial orientation $\theta_0$ affects the trajectory of Janus drops for other angles. Figure 6 presents the dynamics of a dumbbell-shaped Janus drop at $\theta_0 = \pi/6$, $Ca = 0.2$ and $Re = 0.5$, in terms of drop shapes and time variations of $\theta$, $\phi$, and the geometric parameters of the drop. In particular, figure 6(*a*) shows the snapshots of the Janus drop evolving from its initial state to the tumbling regime. Figure 6(*b*) quantifies the process through the temporal evolution of the orientation angles $\theta$ and $\phi$. It is clear that $\theta$ increases with time in an oscillatory manner ($0 \leqslant \dot{\gamma}t < 50$) until the drop enters the tumbling regime ($\dot{\gamma}t > 50$), i.e. the orbit of $\theta = \pi/2$ in figure 4(*a*). The oscillation of $\theta$ is related to the drop rotation, of which the period may vary with time and can be defined by the change of $\phi$ by $2\pi$. Accordingly, the period of the $k$th rotation represents the duration of $2(k-1)\pi \leqslant \phi \leqslant 2k\pi$. Concurrently with the $\theta$-increase, we observe enhanced drop deformation and an expanding projected area in the $x-y$ plane, as evidenced by the variation of $L$ and $\sqrt{R_a R_b}$ in figure 6(*c*). Figure 6(*c*) also indicates that the maxima in $L$ coincide with the minima in $\sqrt{R_a R_b}$, and *vice versa*.

Compared with dumbbell-shaped Janus drops, the initial orientation exerts a fundamentally different influence on the near-spherical Janus drops. Figure 7 shows the orbit evolution of a near-spherical Janus drop in shear flow at $\theta_0 = \pi/6$, $Ca = 0.05$ and $Re = 1$ with respect to the temporal variation of $\theta$. We note that the global deformation



https://doi.org/10.1017/jfm.2025.10988 Published online by Cambridge University Press

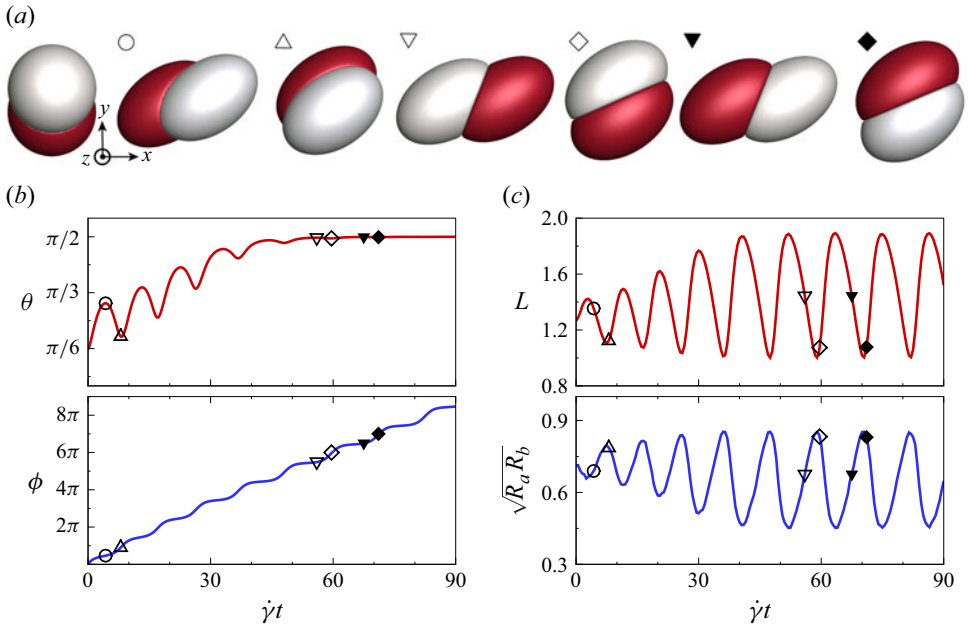



Figure 6. Dynamics of a 3-D tumbling Janus drop in shear flow at $\theta_0 = \pi/6$, $Ca = 0.2$, $Re = 0.5$ and $\sigma_{12} = \sigma_{13}$, in terms of the snapshots of ($a$) interface evolution, ($b$) temporal evolution of $\theta$ and $\phi$, and ($c$) the major semi-axis $L$ and $\sqrt{R_a R_b}$. The symbols correspond to $\dot{\gamma}t = 4.3$ (◯), 8.0 (△), 56.0 (▽), 59.6 (◇), 67.5(▼), 71.1 (◆).

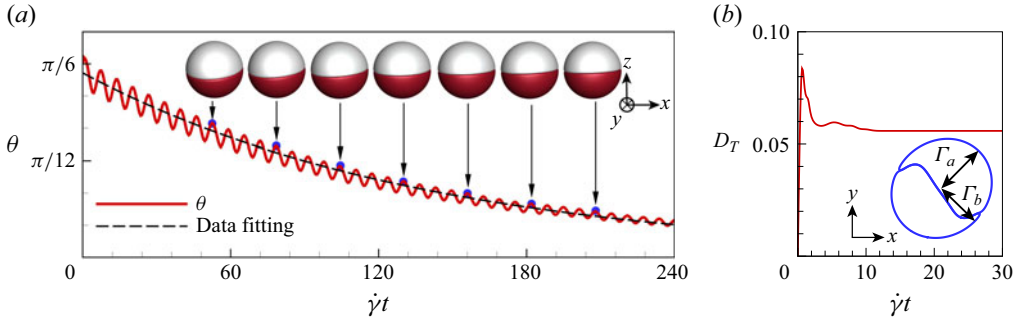



Figure 7. ($a$) Dynamics of near-spherical Janus drops in shear flow at $Ca = 0.05$, $Re = 1$ and $\theta_0 = \pi/6$. The snapshots from left to right correspond to the times $\dot{\gamma}t = 52.5$, 78.5, 104.5, 130.0, 156.0, 182.0 and 208.0. The dashed line indicates the asymptotic approach of $\theta$ to zero by data fitting of $\theta = 0.5\exp(-0.0072\dot{\gamma}t)$. ($b$) Time evolution of the deformation parameter $D_T = (\Gamma_a - \Gamma_b)/(\Gamma_a + \Gamma_b)$.

of drop stabilises after the startup stage (approximately at $\dot{\gamma}t = 12.0$) (figure 7$b$), with the outer interfaces conforming to the streamlines in the surrounding shear flow. The temporal evolution of $\theta$ exhibits an oscillatory decay, gradually decreasing over time with diminishing oscillation amplitude. Although $\theta$ does not reach zero within the extended computation period, its trajectory strongly suggests an asymptotic approach to zero ($\theta = 0.5\exp(-0.0072\dot{\gamma}t)$ by data fitting, see figure 7$a$). This implies that the drop will ultimately enter the spinning regime. More dynamic evolution of orbit drift are provided in the supplementary movies available at https://doi.org/10.1017/jfm.2025.10988.



https://doi.org/10.1017/jfm.2025.10988 Published online by Cambridge University Press

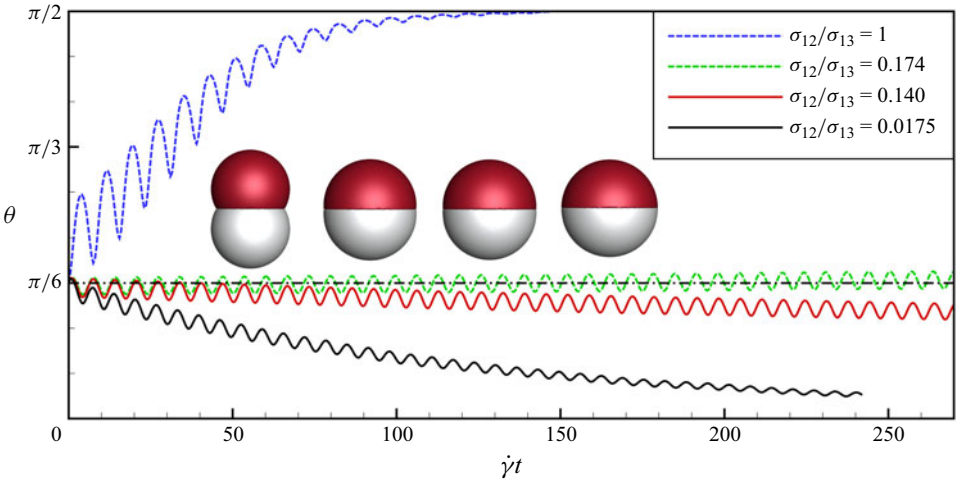



Figure 8. Orbit drift of Janus drops in terms of $\theta$ versus time at $Re = 1$, $Ca = 0.05$, $\theta_0 = \pi/6$ and different values of $\sigma_{12}/\sigma_{13}$. The drop snapshots in the middle of the figure correspond to the drop shapes at equilibrium, with decreasing value of $\sigma_{12}/\sigma_{13}$ from left to right.

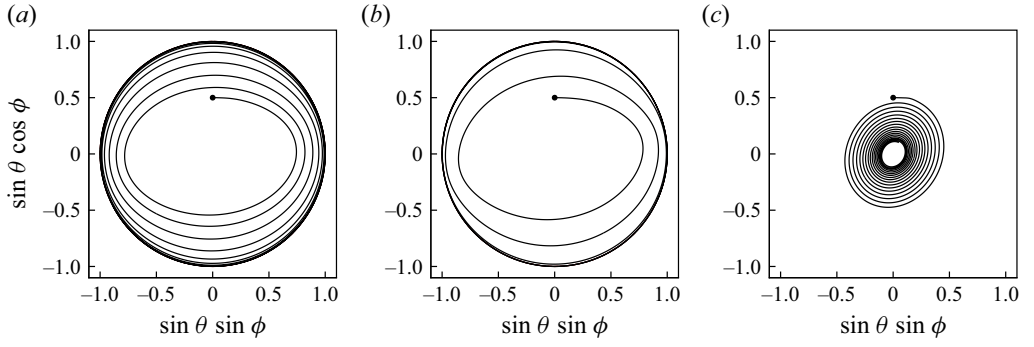



Figure 9. Orbit drift of Janus drops in the $x$–$y$ plane at $Re = 0.5$ and $\theta_0 = \pi/6$. Dumbbell-shaped Janus drops with ($a$) $Ca = 0.05$ and ($b$) $Ca = 0.15$. ($c$) Near-spherical Janus drop with $Ca = 0.05$ and $Re = 1$. Filled circles indicate the initial state of the drop.

### 3.3. *Orbit drift: mechanisms and dynamics*

The bifurcation in orbit drift originates from fundamental differences in deformation dynamics and shape-dependent hydrodynamics between the dumbbell-shaped and near-spherical Janus drops. Specifically, dumbbell-shaped Janus drops exhibit orbit drift dominated by the coupling between the outer interface deformation and the surrounding flow field, steering them towards $\theta = \pi/2$. In contrast, near-spherical drops show orbit drift governed by the interplay between the inner interface deformation and the vortex enclosed within the drop, directing them towards $\theta = 0$. For the dumbbell-shaped cases, the rotation dynamics of drops resembles that of ellipsoids with various aspect ratios in shear flow. The shear-induced global deformation effectively increases the drop aspect ratio (see more details in § 3.4), driving it to higher orbit angles ($\theta$). This elevation further intensifies shear and deformation – a feedback mechanism causing orbit drift towards the tumbling regime. It is noteworthy that in the present study, the tumbling regime occurs for $\theta_0 \neq 0$ (specifically, $\pi/36 \leqslant \theta_0 \leqslant \pi/2$), suggesting that the spinning



https://doi.org/10.1017/jfm.2025.10988 Published online by Cambridge University Press

regime at $\theta_0 = 0$ is unstable. For the near-spherical cases, both the surrounding flow field and the shape of the outer interface enter a steady state during the orbit drift, and the rotation of the inner interface is primarily driven by the hydrodynamic torque from the vortex enclosed within the drop (see figure 5*a*). Moreover, the asymmetry of the inner interface about the $z = 0$ plane leads to an unbalanced torque, thereby inducing a slow orbit drift towards $\theta = 0$ (where the hydrodynamic torque vanishes). Based on the above-mentioned analysis, the tumbling regime at $\theta_0 = \pi/2$ is essentially unstable for near-spherical Janus drops, since any perturbation on the inner interface would trigger the orbit drift towards the spinning regime. Figure 8 shows the orbit drift of Janus drops in terms of $\theta$ versus time at $Re = 1$, $Ca = 0.05$, $\theta_0 = \pi/6$ and different values of $\sigma_{12}/\sigma_{13}$. We can see that $\theta$ increases very slowly with time for $\sigma_{12}/\sigma_{13} = 0.174$, while decreases slowly for $\sigma_{12}/\sigma_{13} = 0.140$. Compared with the cases with extreme surface tension ratios such as $\sigma_{12}/\sigma_{13} = 1$ (dominated by outer interface deformation) and $\sigma_{12}/\sigma_{13} = 0.0175$ (dominated by inner interface deformation), the combined effect of the two mechanisms in these intermediate cases yields significantly slower orbit drift.

The orbit of a Janus drop can be quantitatively described by the projection of the unit vector of $\boldsymbol{d}$ onto the $x$–$y$ plane, i.e. $(\sin\theta\sin\phi, \sin\theta\cos\phi)$. Figure 9 shows the orbit evolution of Janus drops at $\theta_0 = \pi/6$. Given initially $\theta = \pi/6$ and $\phi = 0$, the starting point of the orbit is located at (0, 0.5). For the dumbbell-shaped Janus drops with $Re = 0.5$, the orbit then gradually migrates from the lower polar angle to the higher one, ultimately aligning with that of $\theta = \pi/2$ when reaching the tumbling regime. Furthermore, the drop at relatively high $Ca$ ($= 0.15$) requires less rotation periods to reach the tumbling regime than at relatively low $Ca$ ($= 0.05$). The orbit evolution of the near-spherical Janus drop with $Ca = 0.05$ and $Re = 1$ is in sharp contrast to that of dumbbell-shaped ones: it gradually drifts towards (0, 0). Therefore, it is reasonable to expect that the deformation history of the Janus drop can have a significant effect on the orbit drift.

Figure 10 shows the temporal evolution of the polar angle $\theta$ with various $Ca$, $Re$ and $\theta_0$. Several observations can be made. First, the variation of $\theta$ with time is not a monotonic process, but characterised by periodic oscillations, which is very similar to the orbit drift of a spheroid in shear flow (Mao & Alexeev 2014). Second, Janus drops reach the tumbling regime more rapidly with the increasing of $\theta_0$. Furthermore, if the curves of various $\theta_0$ are shifted to align with that of $\theta_0 = \pi/12$ according to the time reaching the tumbling regime, all the shifted curves collapse onto a single one (see figures 10*b*, 10*d* and 10*f*). In other words, the initial polar angle essentially has no effect on the orbit dynamics, while the start-up effect of Janus drops in shear flow at relatively large $Ca$ might slightly affect the alignment (figure 10*d*). However, this is not surprising, considering the flows are essentially Stokes flow. Third, the comparison between figures 10(*b*) and 10(*d*) shows that drop deformation of Janus drops speeds up the progression of the polar angle towards $\pi/2$. At last, the orbit drift speeds up with increasing inertia (from the comparison between figures 10*c* and 10*e*), similar to ellipsoids in shear flow (Di Giusto *et al.* 2024).

### 3.4. *Effective aspect ratio of dumbbell-shaped Janus drops*

To evaluate the deformation of dumbbell-shaped Janus drops in the tumbling regime, we define an aspect ratio $\lambda = L/\sqrt{R_a R_b}$, where $L$ represents the semi-major axis of the Janus drop, and $R_a$ and $R_b$ denote the long and short radii of the inner interface of component drops, respectively (see the definition in figure 1*b*). For the convenience of discussion, we fix $\theta_0 = \pi/6$ in the following studies. The aspect ratio of a Janus drop at rest, $\lambda_0$, is determined by $\sigma_{12}$ and $\sigma_{13}$ in the present set-up, and can be expressed as (see Appendix A)

https://doi.org/10.1017/jfm.2025.10988 Published online by Cambridge University Press

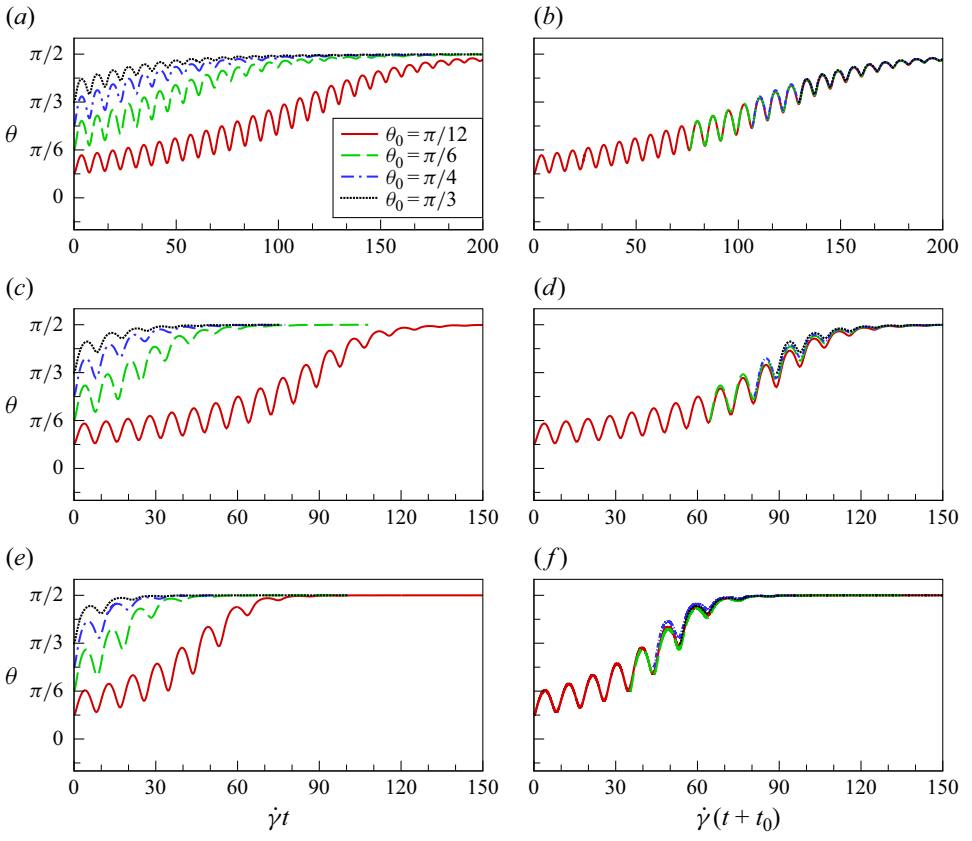



Figure 10. Temporal evolution of $\theta$ for dumbbell-shaped Janus drops: ($a$, $b$) $Re = 0.5$ and $Ca = 0.05$, ($c$, $d$) $Re = 0.5$ and $Ca = 0.15$, ($e$, $f$) $Re = 1.5$ and $Ca = 0.15$. Note that panels ($b$), ($d$) and ($f$) correspond to the results with certain time offsets of panels ($a$), ($c$) and ($e$), respectively. Specifically, for $\theta_0 = \pi/12$, $\pi/4$ and $\pi/3$, the time offsets are $t_0 = 0$, 76.2, 106.8 and 129.7 in panel ($b$), $t_0 = 0$, 64.4, 80.8 and 80.8 and 89.2 in panel ($d$), and $t_0 = 0$, 38.5, 69.3 and 92.4 in panel ($f$), respectively.

$$\lambda_0 = \sqrt{\frac{2\sigma_{13} + \sigma_{12}}{2\sigma_{13} - \sigma_{12}}}. \tag{3.1}$$

It is straightforward to obtain $\lambda_0 = \sqrt{3}$ for $\sigma_{12} = \sigma_{13}$. Figure 11($a$) shows the typical evolution of $\lambda$ in the tumbling regime at $Re = 0.2$, $\theta_0 = \pi/6$ and various $Ca$. The variation of $\lambda$ is periodic with time, and characterised by its maximum and minimum values, denoted by $\lambda_{max}$ and $\lambda_{min}$, respectively. Moreover, the drop experiences linear deformation at small $Ca$ ($= 0.02$) such that $\lambda_0 \approx (\lambda_{max} + \lambda_{min})/2$, while encounters nonlinear deformation at relatively large $Ca$ ($= 0.15$), where $\lambda_{max} - \lambda_0 \gg \lambda_0 - \lambda_{min}$. This implies that the drop deformation is dominated by elongation and thus can be represented by $\lambda_{max}$. The dimensionless rotating period, $\dot{\gamma} t_R$, is related to the drop shape at equilibrium and the drop deformation, as depicted in figures 11($b$) and 11($c$). More specifically, $\dot{\gamma} t_R$ increases with both $\lambda_0$ and $\lambda_{max}$, and is not sensitive to $Re$ at low $Ca$ (e.g. $Ca = 0.02$ and 0.05).

Considering the dynamic similarity between Janus drops and spheroids in shear flow, we tentatively use Jeffery's theory (Jeffery 1922) to predict $t_R$ by introducing an effective



https://doi.org/10.1017/jfm.2025.10988 Published online by Cambridge University Press

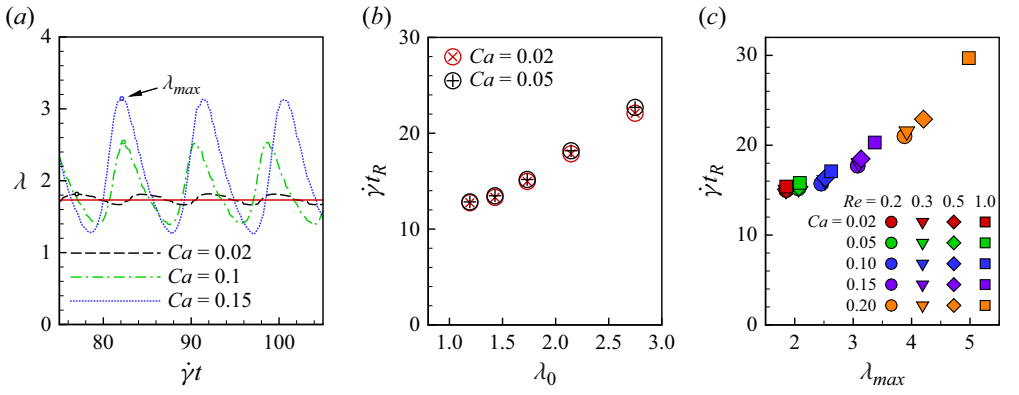



Figure 11. (*a*) Temporal evolution of $\lambda$ at $Re = 0.2$ and various $Ca$. The solid straight line denotes $\lambda_0$. (*b*) $t_R$ versus $\lambda_0$ at $Re = 0.2$ and various $Ca$. (*c*) $t_R$ versus $\lambda_{max}$ at various $Ca$ and $Re$. In panels (*a*) and (*c*), $\lambda_0 = \sqrt{3}$.

aspect ratio $\lambda_e$, such that

$$t_R = \frac{2\pi}{\dot{\gamma}}\left(\lambda_e + \lambda_e^{-1}\right). \tag{3.2}$$

Similarly, the rotational angular velocity $\omega$ ($= \mathrm{d}\phi/\mathrm{dt}$) can be estimated by

$$\omega = \dot{\gamma}\left(\frac{\sin^2\phi + \lambda_e^2\cos^2\phi}{1+\lambda_e^2}\right). \tag{3.3}$$

Note that $\lambda_e$ should take account of the effect of the drop shape at equilibrium $\lambda_0$ and drop deformation (characterised by $\lambda_{max}$), and that its value should lie between $\lambda_0$ and $\lambda_{max}$. Therefore, we tentatively propose

$$\lambda_e = (1-\beta)\lambda_0 + \beta\lambda_{max}, \tag{3.4}$$

where $0 \leqslant \beta \leqslant 1$ is an unknown constant. It is noteworthy that $\lambda_e$ in (3.4) differs from its counterpart for 2-D Janus drops, $\lambda_e^{\text{2-D}} = \lambda_{max}/\lambda_0$ (Zhang *et al.* 2023). In the 2-D case, it is drop deformation that determines the change in aspect ratio and consequently the rotation period, while the equilibrium shape of the drop has insignificant effect (Zhang *et al.* 2023).

To determine the value of $\beta$ and validate the model for $\lambda_e$, we compare $t_R$ obtained from numerical simulations and model predictions based on (3.2), and the results are shown in figure 12(*a*). We find that the model with $\beta = 0.6$ accurately predicts $t_R$ for tumbling Janus drops in the range of parameters considered, which are the same as in figure 11(*b*, *c*). Furthermore, figure 12(*b–e*) presents the comparison of $\omega$ versus $\phi$ between the numerical results at $Re = 0.5$ and the analytical solution of (3.3) using $\lambda_e$ with $\beta = 0.6$. At small $Ca$ ($= 0.02$ and $0.05$), the effect of drop deformation on $\lambda_e$ is insignificant ($\lambda_e/\lambda_0 = 1.04$ and $1.11$, respectively), and the angular velocity $\omega$ virtually overlaps with the model prediction. With further increase of $Ca$ (e.g. $Ca = 0.2$ and $\lambda_e/\lambda_0 = 1.85$), the numerical results deviate from the model prediction, primarily because the drop deformation becomes progressively nonlinear with increasing $Ca$ (Zhang *et al.* 2023). It is interesting to note that a higher effective aspect ratio results in a lower maximum value of $\omega$, which is opposite to the cases of prolate ellipsoids (Daghooghi & Borazjani 2015).



https://doi.org/10.1017/jfm.2025.10988 Published online by Cambridge University Press

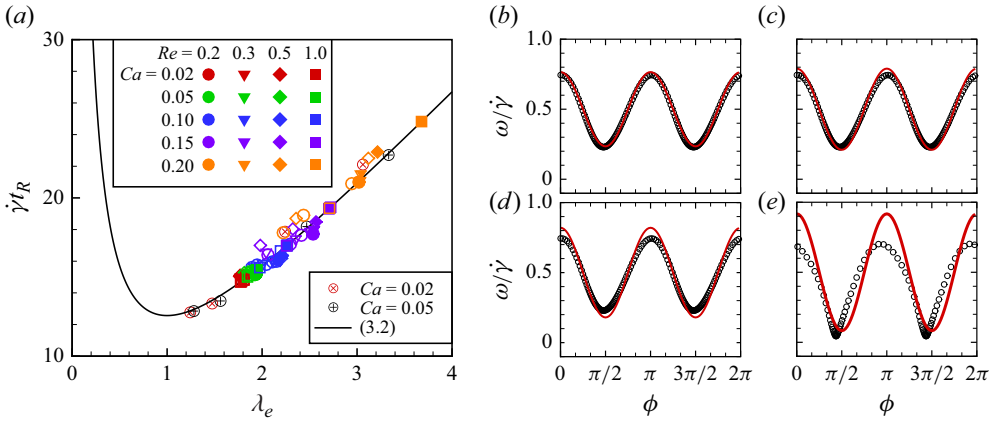



Figure 12. (*a*) Comparison of $t_R$ between numerical results and model prediction of (3.2) (denoted by the solid line). The cases with different $\lambda_0$ are the same as in figure 11(*b*), including $Ca = 0.02$ (⊗) and 0.05 (⊕) at $Re = 0.2$. Other cases correspond to Janus drops with $\sigma_{12} = \sigma_{13}$, covering various $Re$ (= 0.2 (●), 0.3 (▼), 0.5 (♦) and 1 (■)), and various $Ca$ (indicated by colours). For each case, solid symbols regime is as in figure 11(*c*), while hollow symbols correspond to $t_R$ in the orbital drift. (*b*)–(*e*) $\omega$ versus $\phi$ at $Re = 0.5$ and various $Ca$: (*b*) 0.02; (*c*) 0.05; (*d*) 0.1 and (*e*) 0.2. Symbols denote the numerical results and solid curves denote the prediction of (3.3). The effective aspect ratios from panels (*b*) to (*e*) are $\lambda_e = 1.81$, 1.93, 2.21 and 3.21, respectively.

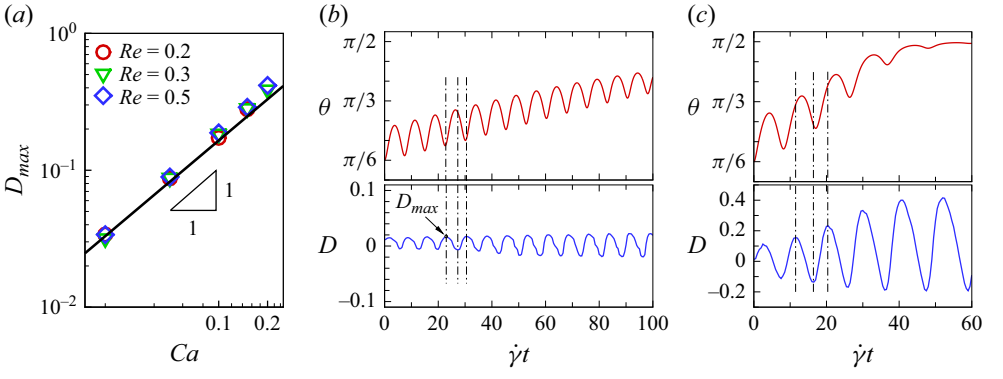



Figure 13. (*a*) $D_{max}$ versus $Ca$ in the tumbling regime. (*b*, *c*) Orbit drift at $Re = 0.5$ and various $Ca$: (*b*) $Ca = 0.02$ and (*c*) $Ca = 0.2$, in terms of evolution of $\theta$ and $D$.

### 3.5. *Effect of deformation on orbit drift of dumbbell-shaped drop*

We define a parameter $D$ to quantitatively measure the drop deformation

$$D = \frac{\lambda - \lambda_0}{\lambda + \lambda_0}. \tag{3.5}$$

Specifically, $D = 0$ corresponds to the Janus drop at equilibrium and $D_{max} = (\lambda_{max} - \lambda_0)/(\lambda_{max} + \lambda_0)$. It is easy to obtain from (3.4) and the definition of $D_{max}$,

$$\frac{\lambda_e}{\lambda_0} = 1 + \frac{2\beta D_{max}}{1 - D_{max}}. \tag{3.6}$$

Figure 13(*a*) indicates $D_{max} \propto Ca$ at relatively small $Ca$ ($\leqslant 0.1$) for Janus drops in the tumbling orbit, consistent with linear deformation of 2-D Janus drops (Zhang *et al.* 2023) and 3-D pure drops in shear flow (Liu *et al.* 2021). Figure 13(*b*, *c*) presents the time



https://doi.org/10.1017/jfm.2025.10988 Published online by Cambridge University Press

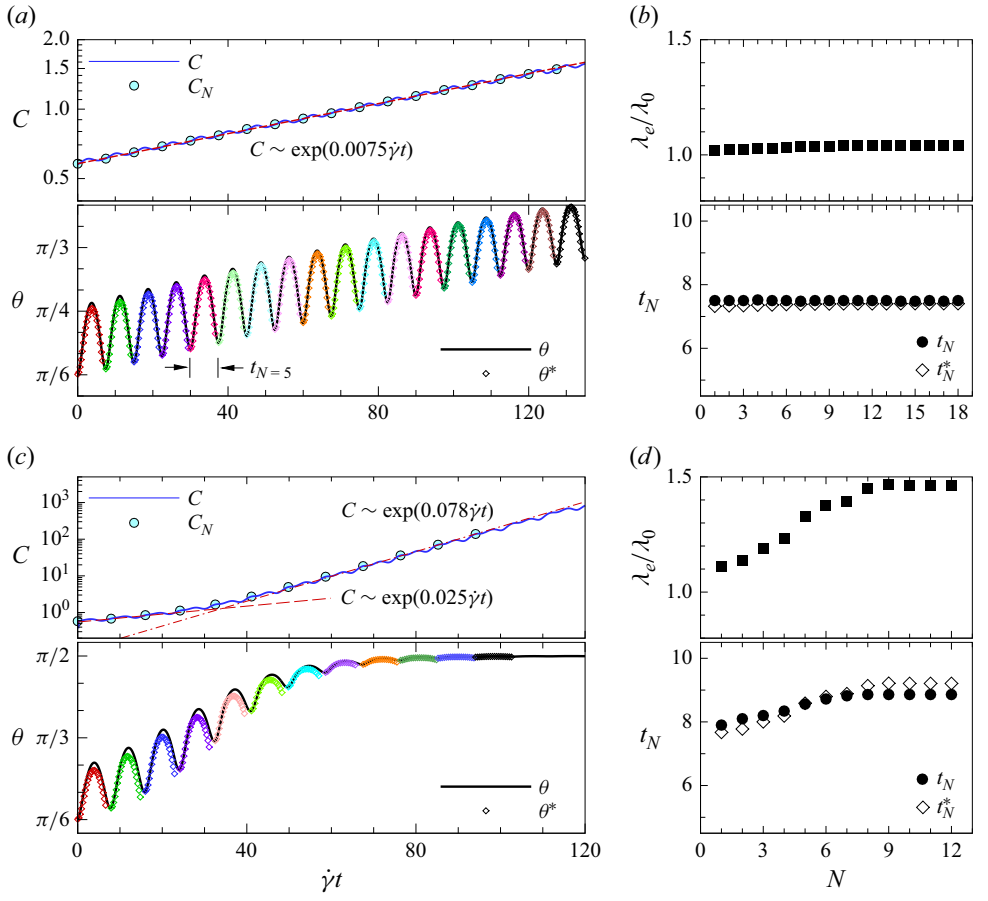



Figure 14. Evolution of orbit parameter $C$, polar angle $\theta$, $\lambda_e$ and $t_N$ of the dumbbell-shaped Janus drops at $Re = 0.2$ and various $Ca =$($a$, $b$) 0.02 and ($c$, $d$) 0.15. In panel ($a$), the variation of $C$ with time follows $C \sim \exp(0.0075\dot{\gamma}t)$. In panel ($b$), the variation of $C$ has two trends: $C \sim \exp(0.078\dot{\gamma}t)$ and $C \sim \exp(0.025\dot{\gamma}t)$. In panels ($b$) and ($d$), $t_N^* = \pi(\lambda_e + \lambda_e^{-1})/\dot{\gamma}$.

evolution of $\theta$ and $D$ at $Re = 0.5$ and various $Ca$ ($= 0.02$ and 0.2, respectively). For the drop with linear deformation ($Ca = 0.02$), the orbit drift takes place slowly, and the variations of $\theta$ and $D$ are apparently coupled in an anti-phase manner: the peak of $D$ coincides with the trough of $\theta$. By contrast, for the drop with nonlinear deformation ($Ca = 0.2$), $D_{max}$ increases more quickly with time and converges to a constant value within 2–3 rotation periods (or entering the tumbling regime). Owing to the significant deformation, the vector $\boldsymbol{d}$ is not perpendicular to the inner interface (see figure 6), and $\theta$ and $D$ do not vary in an anti-phase manner anymore.

To quantitatively assess the effect of drop deformation on the orbit drift, we calculate $\lambda_e$ in each half-period of rotation in the orbit drift, based on (3.4) and $\lambda_{max}$ in the corresponding half-period. Here, the $N$th half-period of rotation is denoted by $t_N$, and defined as $(N-1)\pi \leqslant \phi \leqslant N\pi$; an example $t_{N=5}$ is displayed in figure 14($a$). Note $t_R = t_{N=2k-1} + t_{N=2k}$ for the Janus drop in the $k$th rotation period. Then, we calculate the orbit parameter $C = \lambda_e^{-1} \tan\theta(\sin^2\phi + \lambda_e^2 \cos^2\phi)^{1/2}$ of rotating Janus drops, by integrating $\lambda_e$, $\theta$ and $\phi$ obtained from numerical simulations into (1.1). In turn, we can provide a

https://doi.org/10.1017/jfm.2025.10988 Published online by Cambridge University Press

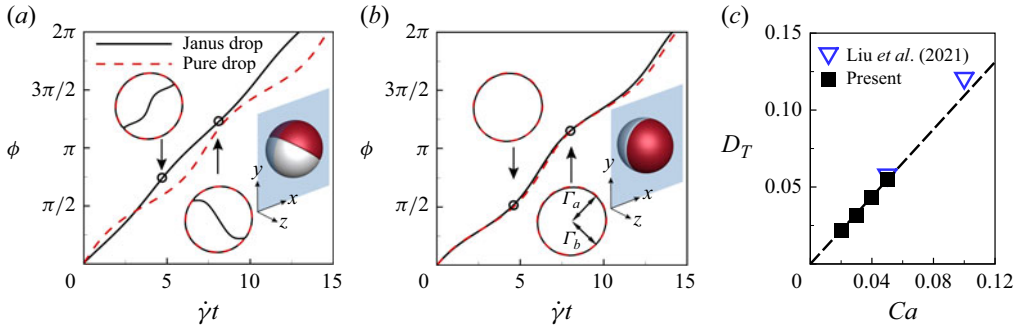



Figure 15. Temporal evolution of $\phi$ for near-spherical Janus drops and pure drops at $Re = 0.5$, $Ca = 0.02$ and different initial orientations: (*a*) $\theta_0 = \pi/2$ and (*b*) $\theta_0 = 0$. The 2-D snapshots of Janus drop in the $x-y$ plane at $z = 0$ are superimposed by that of the pure drop. (*c*) Taylor deformation parameter $D_T$ as a function of $Ca$. Solid symbols denote the present results, hollow ones represent the results of Liu *et al.* (2021) and the dashed line corresponds to $D_T = (35/32)Ca$.

prediction of the polar angle, $\theta^* = \arctan[C_N\lambda_e/(\sin^2\phi^* + \lambda_e^2\cos^2\phi^*)^{1/2}]$, in each half-period of rotation, where $\phi^* = \arctan[\lambda_e\tan(\dot{\gamma}(t-t_0)/(\lambda_e+\lambda_e^{-1}))]$, $t_0$ and $C_N$ denote the starting time and the characteristic orbit parameter of the half-period.

Figure 14 shows the process of orbit drift at $Re = 0.2$ and two $Ca$ ($= 0.02$ and $0.15$), in terms of time evolution of $C$, $\theta$, $\lambda_e$ and $t_N$. At small $Ca$ ($= 0.02$), the Janus drop drifts towards the tumbling orbit, accompanied by the increase of $C$ in an oscillatory way. This remarkably resembles the orbit drift of prolate spheroids in shear flow (Subramanian & Koch 2006). Moreover, we find that the time variation of $C$ generally follows an exponential function, $\exp(\eta\dot{\gamma}t)$ (figure 14*a*), where $k$ ($= 0.0075$) is a constant. Because of insignificant drop deformation ($1 \leqslant \lambda_e/\lambda_0 \leqslant 1.03$), $t_N$ is more or less the same and can be well predicted by Jeffery's theory (3.2) with $\lambda_e = 1.03\lambda_0$ (figure 14*b*). At all times, the prediction of $\theta^*$ is in excellent agreement with the numerical results of $\theta$ (figure 14*a*). At relatively large $Ca$ ($= 0.15$), the time variation of $C$ appears to transit from one exponential function of relatively low $\eta$, $\exp(0.078\dot{\gamma}t)$ for $N \leqslant 2$, to another one of relatively high $\eta$, $\exp(0.025\dot{\gamma}t)$ for $N \geqslant 8$ (figure 14*c*). Clearly, a higher value of $k$ results in a faster orbit drift. Such transition is closely related to the drop deformation: the values of $\lambda_e$ are very close for $N \leqslant 2$ and apparently saturated from $N = 8$. Interestingly, the half-period of rotation during the orbit drift also agrees with the relation in (3.2) (figure 14*d*), which is initially obtained from tumbling Janus drops.

### 3.6. *Deformation of near-spherical Janus drops*

Near-spherical Janus drops in shear flow exhibit deformation behaviour remarkably similar to pure drops. Figures 15(*a*) and 15(*b*) show the time variation of the azimuthal angle $\phi$ for a surface tracer particle (in the $x-y$ plane at $z = 0$) over one period for tumbling and spinning near-spherical Janus drops, respectively. Simulations of a pure drop in shear flow with identical parameters (volume, density, viscosity and surface tension $\sigma_{13}$) confirm that the shapes of Janus and pure drops overlap, independent of the flow regime (tumbling or spinning). However, the tracer particle completes one revolution in a shorter time on the tumbling Janus drop (13.06) compared with the pure drop (14.65), while the spinning Janus and pure drops share roughly the same period. This accelerated motion in the tumbling regime arises from the hydrodynamic torque on the inner interface due to the enclosed vortex within the Janus drop. To quantify the global deformation of the near-spherical Janus drop, we compute the deformation parameter $D_T = (\Gamma_a - \Gamma_b)/(\Gamma_a + \Gamma_b)$



https://doi.org/10.1017/jfm.2025.10988 Published online by Cambridge University Press

in the same way for pure drops, where $\Gamma_a$ and $\Gamma_b$ are semi-major and semi-minor axes of the deformed drop. Figure 15($c$) shows the numerical results of deformation of Janus drops in shear flow at $Re = 0.5$ with respect to $D_T$ versus $Ca$, along with those for 3-D pure drops: theoretical prediction ($D_T = 35Ca/32$) (Taylor 1932) and numerical solutions (Liu *et al.* 2021). Clearly, a good agreement has been achieved, confirming the equivalent deformation dynamics.

## 4. Conclusion

The orbit dynamics of 3-D Janus drops in shear flow has been numerically investigated for dumbbell-shaped and near-spherical drop configurations. We find that dumbbell-shaped drops eventually evolve into the tumbling regime, while near-spherical drops enter the spinning regime. We attribute this bifurcation in orbit drift to contrasting deformation dynamics and shape-dependent hydrodynamics of the two configurations. For the dumbbell-shaped drops, the shear-induced global deformation effectively increases the drop aspect ratio, driving it to the higher orbit angle. This elevation further intensifies shear and deformation – a feedback mechanism causing orbit drift towards the tumbling regime. For the near-spherical drops, the rotation of the inner interface is driven by the hydrodynamic torque from the vortex enclosed within the drop. The asymmetry of the inner interface about the $z = 0$ plane leads to an unbalanced torque, thereby inducing a slow orbit drift towards the spinning regime.

For the dumbbell-shaped Janus drops, the tumbling dynamics is found to resemble ellipsoids with different aspect ratios. Moreover, the drop trajectories during orbit drift collapse onto a universal curve, independent of the initial orientations; significant deformation and inertia accelerate the orbit transition. To describe the effect of drop deformation on the orbit drift, we examine the deformation behaviour of dumbbell-shaped Janus drops at various capillary number and observe that the magnitude of drop deformation effectively increases with the orbit, as well as the effective aspect ratio. Accordingly, we propose a model for effective aspect ratio, $\lambda_e = \lambda_0 + \beta(\lambda_{max} - \lambda_0)$, in which the drop shapes at equilibrium ($\lambda_0$) and at the maximum elongation ($\lambda_{max}$) are taken into account, and $\beta = 0.6$ is a fitting parameter. Given the similarity in the orbit drift between the particles and the Janus drops, we incorporate the effective aspect ratio into Jeffery's theory for solid particles to predict the orbit dynamics of dumbbell-shaped Janus drops. By comparison with the numerical results, we show that the resulting model can accurately predict the rotation period and angular velocity of Janus drops in the tumbling regime and during the orbit drift, especially for the drops with linear deformation. Finally, we find that the orbit parameter $C$ varies exponentially with time for the drops with linear deformation, while the time variation of $C$ transits from one exponential function to another for drops with nonlinear deformation.

In the present study, we only consider the Janus drops with two symmetrical component drops. Any difference in density, viscosity, surface tension coefficient and volume between the two component drops would introduce new asymmetries to the flow, and give rise to more complex dynamics of the Janus drops, which will be our future research topics.

**Supplementary movies.** Supplementary movies are available at https://doi.org/10.1017/jfm.2025.10988.

**Funding.** We are grateful for the support of the National Natural Science Foundation of China (grant numbers: 12388101, 12241204, 12302342, 11932019).

**Declaration of interests.** The authors report no conflict of interest.

**Author contributions.** J.-Q. C. and C.-Y. Z. have contributed equally to the article.



https://doi.org/10.1017/jfm.2025.10988 Published online by Cambridge University Press

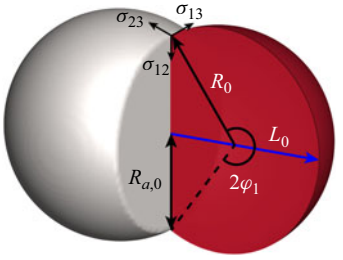



Figure 16. Sketch of a 3-D Janus drop at equilibrium.

## Appendix A. Calculation of the initial aspect ratio $\lambda_0$ and radius $R_0$ for 3-D symmetric Janus drops at equilibrium

The aspect ratio $\lambda_0$ and radius $R_0$ of the 3-D symmetric Janus drops at equilibrium can be calculated by the surface tension coefficient $\sigma_{ij}$ between the $i$th and $j$th fluid. A sketch of the interface shape of a 3-D symmetric Janus drop at equilibrium is shown in figure 16. The interfacial angles of fluid $i$ (= 1, 2 or 3) are represented by $\varphi_i$. Clearly, $\varphi_1 + \varphi_2 + \varphi_3 = 2\pi$. A balance of surface tensions at the triple-phase line can be written as (Zhang *et al.* 2021)

$$\frac{\sin\varphi_1}{\sigma_{23}} = \frac{\sin\varphi_2}{\sigma_{13}} = \frac{\sin\varphi_3}{\sigma_{12}}. \tag{A1}$$

Given $\sigma_{13} = \sigma_{23}$ for 3-D symmetric Janus drops, we have $\varphi_1 = \varphi_2 = \arccos(-\sigma_{12}/(2\sigma_{13}))$ and $\varphi_3 = 2\pi - 2\varphi_1$.

At equilibrium, the surfaces of the component drops are spherical, with radius $R_0$ and size $2\pi R^3/3$, and the inner interface is a plane circle. Geometrically, the initial semi-major axis of the Janus drop $L_0$ and the radius of the inner interface $R_{a,0}$ (= $R_{b,0}$) yield

$$L_0 = R_0(1 - \cos\varphi_1), \quad R_{a,0} = R_{b,0} = R_0 \sin\varphi_1. \tag{A2}$$

The aspect ratio of a Janus drop is defined as $\lambda_0 = L_0/(R_{a,0}R_{b,0})^{1/2}$. Substituting $L_0$, $R_{a,0}$, $R_{b,0}$ and $\varphi_1$ into the definition of $\lambda_0$, it can be expressed by

$$\lambda_0 = \frac{1 - \cos\varphi_1}{\sin\varphi_1} = \sqrt{\frac{2\sigma_{13} + \sigma_{12}}{2\sigma_{13} - \sigma_{12}}}. \tag{A3}$$

Given that the volume of the component drop yields $\pi(3R_0 - L_0)L_0^2/3 = 2\pi R^3/3$, the initial radius of the component drop can be calculated by

$$R_0 = \frac{2R\sigma_{13}}{\sqrt[3]{(2\sigma_{13} + \sigma_{12})^2(4\sigma_{13} - \sigma_{12})}}. \tag{A4}$$

## References


Abadi, R.H.H., Rahimian, M.H. & Fakhari, A. 2018 Conservative phase-field lattice-Boltzmann model for ternary fluids. *J. Comput. Phys.* **374**, 668–691.

Bonacci, F., Chakrabarti, B., Saintillan, D., du Roure, O. & Lindner, A. 2023 Dynamics of flexible filaments in oscillatory shear flows. *J. Fluid Mech.* **955**, A35.

Chen, J.-W., Zhang, C.-Y., Liu, H.-R. & Ding, H. 2025 Improved phase field model for two-phase incompressible flows: sharp interface limit, universal mobility and surface tension calculation. arXiv:2501.10167.

Cox, R.G. 1971 The motion of long slender bodies in a viscous fluid. Part 2. Shear flow. *J. Fluid Mech.* **45**, 625–657.




https://doi.org/10.1017/jfm.2025.10988 Published online by Cambridge University Press

DABADE, V., MARATH, N.K. & SUBRAMANIAN, G. 2016 The effect of inertia on the orientation dynamics of anisotropic particles in simple shear flow. *J. Fluid Mech.* **791**, 631–703.
DAGHOOGHI, M. & BORAZJANI, I. 2015 The influence of inertia on the rheology of a periodic suspension of neutrally buoyant rigid ellipsoids. *J. Fluid Mech.* **781**, 506–549.
DI GIUSTO, D., BERGOUGNOUX, L., MARCHIOLI, C. & GUAZZELLI, E. 2024 Influence of small inertia on Jeffery orbits. *J. Fluid Mech.* **979**, A42.
DÍAZ-MALDONADO, M. & CÓRDOVA-FIGUEROA, U.M. 2015 On the anisotropic response of a Janus drop in a shearing viscous fluid. *J. Fluid Mech.* **770**, R2.
DING, H., SPELT, P.D.M. & SHU, C. 2007 Diffuse interface model for incompressible two-phase flows with large density ratios. *J. Comput. Phys.* **226**, 2078–2095.
EINARSSON, J., CANDELIER, F., LUNDELL, F., ANGILELLA, J.R. & MEHLIG, B. 2015 Effect of weak fluid inertia upon Jeffery orbits. *Phys. Rev. E* **91**, 041002.
FENG, J. & JOSEPH, D.D. 1995 The unsteady motion of solid bodies in creeping flows. *J. Fluid Mech.* **303**, 83–102.
GOODLING, A.E., NAGELBERG, S., KAEHR, B., MEREDITH, C.H., CHEON, S.I., SAUNDERS, A.P., KOLLE, M. & ZARZAR, L.D. 2019 Colouration by total internal reflection and interference at microscale concave interfaces. *Nature* **566**, 523–527.
GUAZZELLI, E. & POULIQUEN, O. 2018 Rheology of dense granular suspensions. *J. Fluid Mech.* **852**, P1.
GUO, P., ZENG, C.-F., WANG, C.-Q. & ZHANG, L.-X. 2017 Magnetic ionic liquid-water Janus droplets: preparation, structure and morphology adjustment and magnetic manipulation. *AIChE J.* **63**, 4115–4123.
HAO, X., DU, T., HE, H., YANG, F., WANG, Y., LIU, G. & WANG, Y. 2022 Microfluidic particle reactors: from interface characteristics to cells and drugs related biomedical applications. *Adv. Mater. Interfaces* **9**, 2102184.
HARRIS, J.B. & PITTMAN, J.F.T. 1975 Equivalent ellipsoidal axis ratios of slender rod-like particles. *J. Colloid Interface Sci.* **50**, 280–282.
HUANG, H.-B., YANG, X., KRAFCZYK, M. & LU, X.-Y. 2012 Rotation of spheroidal particles in Couette flows. *J. Fluid Mech.* **692**, 369–394.
HWANG, D. & YUN, S. 2023 Bouncing characteristics of Janus drop impact on curved surfaces. *Phys. Fluids* **35**, 062015.
JEFFERY, G.B. 1922 The motion of ellipsoidal particles immersed in a viscous fluid. *Proc. R. Soc. Lond. A* **102**, 161–179.
JUNG, H.J. & YUN, S. 2023 Splitting behavior of Janus drop impact on protrusion structure. *Phys. Fluids* **35**, 062105.
KARNIS, A., GOLDSMITH, H.L. & MASON, S.G. 1963 Axial migration of particles in Poseuille flow. *Nature* **200**, 159–160.
LEAL, L.G. 1980 Particle motions in a viscous-fluid. *Annu. Rev. Fluid Mech.* **12**, 435–476.
LIU, H.-R., NG, C.S., CHONG, K.L., LOHSE, D. & VERZICCO, R. 2021 An efficient phase-field method for turbulent multiphase flows. *J. Comput. Phys.* **446**, 110659.
LIU, W.-K. & PARK, J.M. 2022 Ternary modeling of the interaction between immiscible droplets in a confined shear flow. *Phys. Rev. Fluids* **7**, 013604.
LIU, W.-K. & PARK, J.M. 2023 Numerical study on the engulfing behavior between immiscible droplets in a confined shear flow. *Chem. Engng Sci.* **266**, 118265.
MAO, W. & ALEXEEV, A. 2014 Motion of spheroid particles in shear flow with inertia. *J. Fluid Mech.* **749**, 145–166.
MARATH, N.K. & SUBRAMANIAN, G. 2017 The effect of inertia on the time period of rotation of an anisotropic particle in simple shear flow. *J. Fluid Mech.* **830**, 165–210.
MAUER, J.S., MENDEZ, S., LANOTTE, L., NICOUD, F., ABKARIAN, M., GOMPPER, G. & FEDOSOV, D.A. 2018 Flow-induced transitions of red blood cell shapes under shear. *Phys. Rev. Lett.* **121**, 118103.
OLSSON, E., KREISS, G. & ZAHEDI, S. 2007 A conservative level set method for two phase flow II. *J. Comput. Phys.* **225**, 785–807.
SINGH, V., KOCH, D.L., SUBRAMANIAN, G. & STROOCK, A.D. 2014 Rotational motion of a thin axisymmetric disk in a low Reynolds number linear flow. *Phys. Fluids* **26**, 033303.
SLOWICKA, A.M., STONE, H.A. & EKIEL-JEZEWSKA, M.L. 2020 Flexible fibers in shear flow approach attracting periodic solutions. *Phys. Rev. E* **101**, 023104.
SONG, Q., CHAO, Y., ZHANG, Y. & SHUM, H.C. 2021 Controlled formation of all-aqueous Janus droplets by liquid–liquid phase separation of an aqueous three-phase system. *J. Phys. Chem. B* **125**, 562–570.
SUBRAMANIAN, G. & KOCH, D.L. 2005 Inertial effects on fibre motion in simple shear flow. *J. Fluid Mech.* **535**, 383–414.

https://doi.org/10.1017/jfm.2025.10988 Published online by Cambridge University Press

SUBRAMANIAN, G. & KOCH, D.L. 2006 Inertial effects on the orientation of nearly spherical particles in simple shear flow. *J. Fluid Mech.* **557**, 257–296.
TAYLOR, G.I. 1923 The motion of ellipsoidal particles in a viscous fluid. *Proc. R. Soc. Lond. A* **103**, 58–61.
TAYLOR, G.I. 1932 The viscosity of a fluid containing small drops of another fluid. *Proc. R. Soc. Lond. A* **138**, 41–48.
THORP, I.R. & LISTER, J.R. 2019 Motion of a non-axisymmetric particle in viscous shear flow. *J. Fluid Mech.* **872**, 532–559.
TORZA, S. & MASON, S.G. 1970 Three-phase interactions in shear and electrical fields. *J. Colloid Interface Sci.* **33**, 67–83.
TREVELYAN, B.J. & MASON, S.G. 1951 Particle motions in sheared suspensions. I. Rotations. *J. Colloid Sci.* **6**, 354–367.
VOTH, G.A. & SOLDATI, A. 2017 Anisotropic particles in turbulence. *Annu. Rev. Fluid Mech.* **49**, 249–276.
WANG, H., WANG, S., MU, Y., HAN, Q. & CHENG, Y. 2024 Dynamic breakup of Janus droplet in a bifurcating microchannel. *Phys. Rev. Fluids* **9**, 064203.
YARIN, A.L., GOTTLIEB, O. & ROISMAN, I.V. 1997 Chaotic rotation of triaxial ellipsoids in simple shear flow. *J. Fluid Mech.* **340**, 83–100.
YUN, S., KIM, J. & KIM, G.H. 2022 Dynamic characteristics of ellipsoidal Janus drop impact on a solid surface. *Phys. Fluids* **34**, 102104.
ZHANG, C.-Y., CHEN, J.-L., QIAN, L.-J. & DING, H. 2023 Two-dimensional Janus drops in shear: deformation, rotation and their coupling. *J. Fluid Mech.* **976**, A29.
ZHANG, C.-Y., DING, H., GAO, P. & WU, Y.-L. 2016 Diffuse interface simulation of ternary fluids in contact with solid. *J. Comput. Phys.* **309**, 37–51.
ZHANG, C.-Y., GAO, P., LI, E.-Q. & DING, H. 2021 On the compound sessile drops: configuration boundaries and transitions. *J. Fluid Mech.* **917**, A37.
ZHANG, X. & GRAHAM, M.D. 2020 Multiplicity of stable orbits for deformable prolate capsules in shear flow. *Phys. Rev. Fluids* **5**, 023603.
ZHU, Z.-Q., CHEN, T.-A., ZHU, Y.-Q., HUANG, F.-S., MU, K., SI, T. & XU, R.X. 2023 Programmable pulsed aerodynamic printing for multi-interface composite manufacturing. *Matter* **6**, 2034–2051.

https://doi.org/10.1017/jfm.2025.10988 Published online by Cambridge University Press